UC Davis
UC Davis Previously Published Works

Title

Reduction reactions and densification during in situ TEM heating of iron oxide nanochains

Permalink

https://escholarship.org/uc/item/9jq002b6

Authors

Bonifacio, Cecile S
Das, Gautom
Kennedy, Ian M
et al.

Peer reviewed

Reduction reactions and densification during *in situ* TEM heating of iron oxide nanochains

Cecile S. Bonifacio,[1,a)] Gautom Das,[2] Ian M. Kennedy,[2] and Klaus van Benthem[1,b)]

[1]*Department of Materials Science and Engineering, University of California Davis, 1 Shields Ave., Davis, California 95616, USA*

[2]*Department of Mechanical and Aerospace Engineering, University of California Davis, 1 Shields Ave., Davis, California, 95616, USA*

The reduction reactions and densification of nanochains assembled from γ-Fe$_2$O$_3$ nanoparticles were investigated using *in situ* transmission electron microscopy (TEM). Morphological changes and reduction of the metal oxide nanochains were observed during *in situ* TEM annealing through simultaneous imaging and quantitative analysis of the near-edge fine structures of Fe L$_{2,3}$ absorption edges acquired by spatially resolved electron energy loss spectroscopy. A change in the oxidation states during annealing of the iron oxide nanochains was observed with phase transformations due to continuous reduction from Fe$_2$O$_3$ over Fe$_3$O$_4$, FeO to metallic Fe. Phase transitions during the *in situ* heating experiments were accompanied with morphological changes in the nanochains, specifically rough-to-smooth surface transitions below 500 °C, neck formation between adjacent particles around 500 °C, and subsequent neck growth. At higher temperatures, coalescence of FeO particles was observed, representing densification. *Published by AIP Publishing.*
https://doi.org/10.1063/1.5004092

I. INTRODUCTION

Sintering describes the consolidation of individual (nano) particles to form a dense microstructure, and is commonly achieved by heating and the application of pressure.[1] At high temperatures, sintering in air may be accompanied by oxidation, while reduction of the starting powder often occurs under vacuum conditions. Electric field assisted sintering (EFAS), which includes spark plasma sintering (SPS), field-assisted sintering technology (FAST), and flash sintering, is often characterized by accelerated densification, or lower onset temperatures for densification. During EFAS of metal powders, a "surface cleaning" effect during the initial stage of sintering was suggested that removes oxides and contaminants from the surface of metal powders to promote neck formation and subsequent densification.[2–9] Mechanistic descriptions initially included surface oxide removal by spark or even plasma formation[4,5] and local field amplification.[2,10] Bonifacio and co-workers later used *in situ* transmission electron microscopy (TEM) to demonstrate the electric field-induced dielectric breakdown to be responsible for oxide removal.[11,12] In the absence of any electric fields or current, "surface cleaning" can be accomplished by oxide solution in the metal particles,[8] or reduction-oxidation reactions at elevated temperatures.[13] EFAS of dielectric oxide powders may be impacted by surface impurities that give rise to unintended excess at grain boundaries in the resulting dense microstructures, but surface cleaning effects were heretofore not discussed. To date, limited information is available on reduction-oxidation reactions during densification of dielectric particles.

This study reports reduction-oxidation reactions and sintering mechanisms for nanochains assembled from individual iron oxide particles. *In situ* TEM heating experiments were used to directly observe morphological changes of nanochains with increasing temperatures. Alterations of the Fe oxidation state were monitored by electron energy loss spectroscopy (EELS). Iron oxide was chosen as a model system due to its potential to occur in a number of different valence states, and its technological relevance due to its intriguing magnetic, electronic, photonic, and optical properties.[14] Nanosized iron oxides have shown prospective application in magnetic storage, electronics, gas sensing, biomedical engineering, and catalysis.[15–20] This wide variety of potential applications necessitates a fundamental understanding of its morphological and phase stability.[21] An abundance of reports published in the literature focus on the synthesis of iron oxide nanoparticles with controlled sizes and shapes, but only few studies describe the sintering kinetics of iron oxides. The sintering study by Kramer and German[22] demonstrated the surface diffusion-controlled oxidation of Fe$_3$O$_4$ to α- Fe$_2$O$_3$ above 673 K, which then consolidates more rapidly than Fe$_3$O$_4$.[23,24] Praksh reports that the reduction of iron oxide with heating above 570 °C generates a series of stable phases, ranging from hematite (α-Fe$_2$O$_3$), over maghemite (γ-Fe$_2$O$_3$), magnetite (Fe$_3$O$_4$), and wüstite (FeO).[25] Based on processing conditions, such as different temperatures, pressures, and atmospheres, consolidation of iron ores is complex, and sintering studies must be augmented with phase equilibrium, reduction/oxidation, and diffusion studies.[25]

II. EXPERIMENTAL DETAILS

Iron oxide nanoparticles were synthesized using a H$_2$/air diffusion flame generated in a configuration sketched in Fig. 1(a). The experimental set-up consists of two concentric brass

---

a)Current address: E.A. Fischione Instruments, Inc., 9003 Corporate Circle, Export, PA 15632, USA.
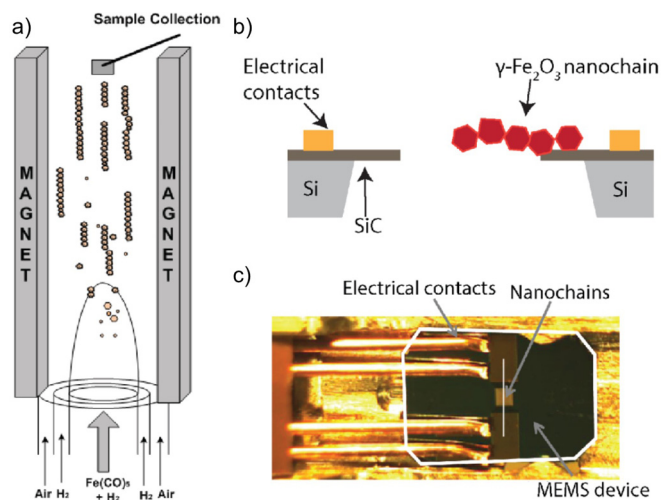
b)Electronic mail: Benthem@ucdavis.edu

FIG. 1. (a) Sketch of the flame synthesis set-up used to synthesize the iron oxide nanochains. (b) is a schematic of the experimental geometry along the cross-section of the MEMS device [dashed line in (c)] with the iron oxide nanoparticles forming the nanochains over the hole on SiC membrane.

tubes, with outer diameters of 14 and 11 mm. Vapor of iron pentacarbonyl [Alfa Cesar, chemical formula $Fe(CO)_5$, decomposition temperature 200 °C] was doped into the H_2 fuel gas to provide the precursor for the nanoparticles.

A pure H_2 stream was mixed with the $Fe(CO)_5$-laden stream before entering the burner. The H_2 carrier gas flowed through the headspace of an airtight $Fe(CO)_5$ container, which was maintained in an ice-water bath to ensure steady concentrations of $Fe(CO)_5$. A stable, self-sustaining laminar diffusion flame was established on the tubular burner. Using this set-up, iron oxide nanoparticles were synthesized using a H_2 flow rate of 0.37 l/min, of which 0.12 l/min was the $Fe(CO)_5$ carrier gas. A 4-channel MKS 647C (MKS Instruments Inc., MA) mass flow controller was used to control the H_2 gas flow. Two bar magnets (300 mT, 10 cm tall) were placed parallel to each with a distance of 30 mm to each other bracketing the flame. The magnets create a uniform magnetic field with field lines directed across the flow regime of the nanoparticles. A constant flame height of 45 mm was maintained throughout the experiments. Iron oxide nanoparticle particles with sizes ranging from 5 to 50 nm in diameter were produced at the tip of the flame. With longer residence time, they align and assemble as nanochains downstream under the applied magnetic field. Samples were thermophoretically collected from the flame at a height of approximately 55 mm from the visible flame tip using the rapid insertion technique. Nanochains were subsequently deposited onto a holey silicon carbide membrane that was supported by monolithic silicon [Fig. 1(b)]. The membrane/Si structure is part of a commercially available micro-electromechanical system (MEMS) device (Protochips Inc., Raleigh, NC), which serves as the sample support for a double-tilt Protochips Aduro sample holder for the *in situ* TEM heating experiments [cf. Fig. 1(c)]. The sample temperature is controlled by resistively heating the SiC membrane during the TEM observation. Temperatures are calibrated against heating currents for each individual MEMS device by the manufacturer using a pyrometer. Due to the small thermal volume of the heating membrane and the nanochains, heating

rates as high as 1000 K/ms are feasible, while cool-down rates are marginally smaller due to thermal conductivity.[26] During the *in situ* experiments, a ramp-up/hold/ramp-down cycles were applied for holding temperatures (T_{hold}) between 200 °C and 900 °C. The ramp-up and ramp-down cycles were applied from and to 25 °C with heating and cooling rates of 5 °C/s, respectively. Holding times were $T_{hold} = 200$ s, which was sufficient to obtain stable temperatures and equilibrium conditions of the nanochains due to their relatively small thermal volume.

TEM experiments were carried out using a JEOL JEM 2500SE TEM and an aberration corrected JEOL JEM 2100F/C_s scanning transmission electron microscope (STEM), both operated at 200 keV. During the *in situ* experiments, TEM images were acquired as video signals. Electron energy loss spectroscopy (EELS) data were recorded at room temperature as line scans across the nanochains in STEM mode, using a Gatan Tridiem parallel electron energy loss spectrometer attached to the aberration-corrected JEOL JEM 2100F/C_s microscope. O K and Fe $L_{2,3}$ ionization edges were acquired with an energy dispersion of 0.3 eV/channel. Spectrum acquisition at room temperature was accomplished by abrupt quenching to room temperature and re-heating with a rate of 1000 K/ms before and after EELS acquisition, respectively. Additional control EELS experiments were carried out with the sample heated at the indicated temperature to confirm accuracy of the presented results. Spectra acquired intermittently at room temperature and at high temperature were indistinguishable from each other apart from differences in signal-to-noise ratio and apparent energy resolution.

The oxidation states of iron after heating at different temperatures were determined from L_3/L_2 intensity ratio calculated from the acquired Fe $L_{2,3}$ ionization edges. The branching ratios were obtained using the method described by Jasinski *et al*.[27] This involved the background subtraction of Fe $L_{2,3}$ spectra using an inverse power law after a pre-edge fitting routine,[28] and subsequent linear baseline background removal underneath the Fe $L_{2,3}$ edge following the methods described by Pearson *et al*.[29] The Fe L_3 and L_2 edges were fitted by either a single or two Gaussian peaks whichever yielded the best quality fit. The L_3/L_2 intensity ratio was subsequently calculated from the ratio of the integrated areas underneath the L_3 and L_2 absorption edges, respectively.

III. RESULTS

A. *In situ* heating

Figure 2 shows faceted iron oxide nanoparticles prior to their assembly in nanochains within an applied magnetic field. A selected area electron diffraction pattern recorded from the same area is displayed on the left side of Fig. 2(b). For more accurate data analysis, the recorded diffraction pattern was rotationally averaged [right side in Fig. 2(b)]. The determined lattice plane spacing for the marked diffraction rings is in excellent agreement with those for γ-Fe_2O_3 published by Jasinski *et al*.[27] and Zhou *et al*.[30] for the same nanoparticles.

The application of a magnetic field across the diffusion flame furnace causes the alignment of the γ-Fe_2O_3 nanoparticles into 1-dimensional nanochains with various lengths.[31]
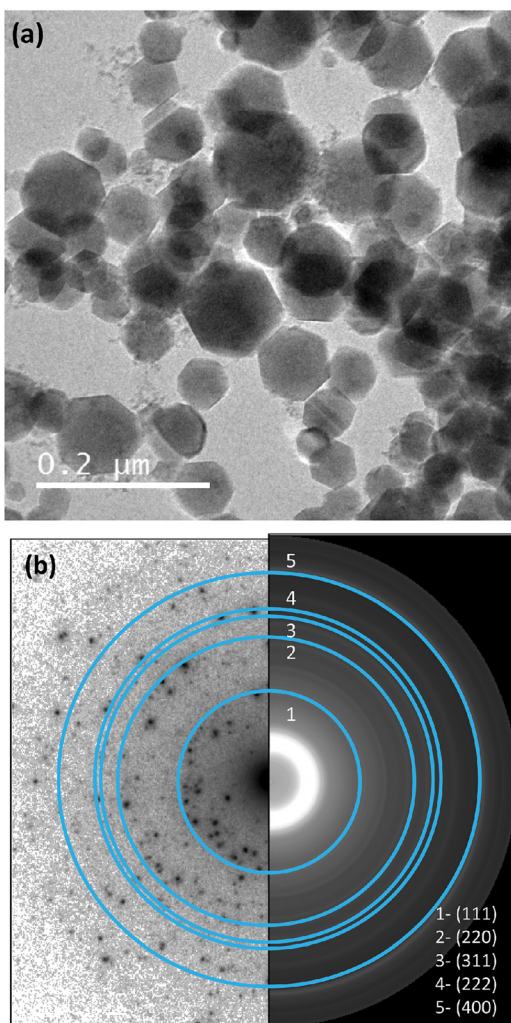
FIG. 2. (a) Bright field TEM micrograph of iron oxide nanoparticles prior to their exposure to a magnetic field. (b) is comprised of a selected area electron diffraction pattern of the same area, and its rotational average. The marked diffraction rings represent lattice planes of the γ-Fe$_2$O$_3$.
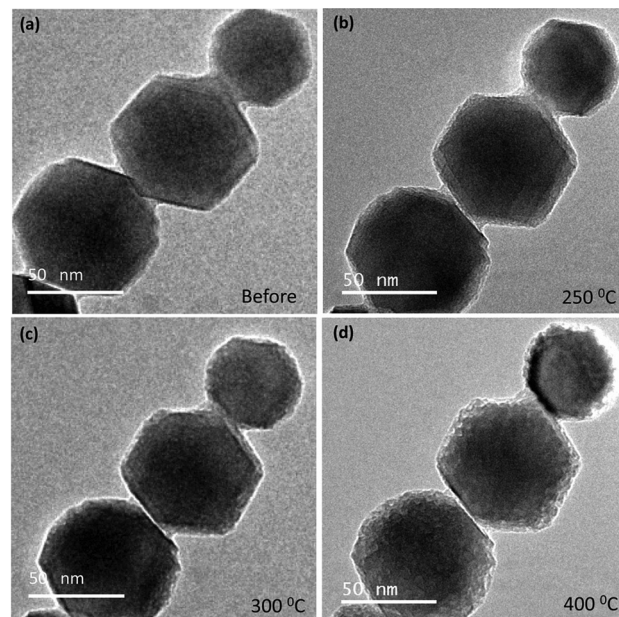

FIG. 3. Series of HRTEM micrographs acquired at different temperatures during *in situ* heating. The rather flat and smooth surface morphology of the nanoparticles at room temperature becomes increasingly rougher with crater-like morphologies starting to emerge between 300 °C and 400 °C.

Figure 3 displays a series of bright field TEM images recorded from a section of one nanochain at different temperatures during an *in situ* heating experiment. The as-synthesized particles exhibit a highly faceted shape [Fig. 3(a)] with smooth surfaces. With increasing temperature, the particles' surface morphology begins to change [Fig. 3(b)] and shows significant roughness once a temperature of 300 °C is reached [Fig. 3(c)]. Upon further heating to 400 °C, crater-like structures on the surface of the nanoparticles become evident [Fig. 3(d)].

Figure 4 shows a series of high-angle annular dark-field (HAADF) STEM images acquired from another particle chain at various temperatures between room temperature and 900 °C. A similarly rough surface morphology as that described above is confirmed for temperatures between 400 °C and 450 °C [Figs. 4(b) and 4(c)], while individual particles are loosely contacting each other without the presence of an extended interparticle neck. Once the temperature exceeded 500 °C, sharp contrast lines between adjacent particles (marked by arrows) indicate the formation of necks, i.e., grain boundaries [*neck 1* in Fig. 4(d) at 500 °C, and *neck 2* in Fig. 4(e) at 650 °C]. In addition, above 500 °C, particle surfaces become smooth

again. Further heating to temperatures above 800 °C–850 °C caused consolidation of the nanochains, as displayed by Fig. 4(d) recorded at 900 °C.

B. EELS analysis

Electron energy-loss near-edge fine structures (ELNES) of the Fe L$_{2,3}$ edges were recorded from various different areas along individual nanochains as a function of temperature during *in situ* heating experiments. Figure 5(a) shows the background-stripped Fe L$_{2,3}$ absorption edges recorded from the center of the nanochains before *in situ* heating, and in between the heating cycles at the specified temperatures between 200 °C and 900 °C. The onset of the L$_3$ edge, as identified by the first inflection point of the ELNES line shape, reveals a shift of 1.4 eV toward lower energy losses when increasing the annealing temperature from 500 °C to 900 °C.

In Fig. 5(b), the corresponding L$_3$/L$_2$ white line intensity ratios determined following the techniques described above are plotted as a function of temperature. After the statistical analysis of multiple line scans acquired from different areas and different samples, the absolute error bars range between 0.1 and 0.2, or 1.5% and 5.5% for temperatures up to 800 °C, while the relative error at 900 °C amounts to 10.5% due to the relatively low L$_3$/L$_2$ ratio.

Above 200 °C, the L$_3$/L$_2$ intensity ratio drops significantly from 6.1 ± 0.1 to 5.0 ± 0.1, and subsequently stabilizes at 4.7 ± 0.1 for temperatures up to 450 °C. Between 450 °C and 800 °C, the observed intensity ratios fluctuate between 3.5 ± 0.2 and 4.3 ± 0.2, and drop dramatically to as low as 1.9 ± 0.2 at 900 °C. The experimentally observed L$_3$/L$_2$ intensity ratios agree well with reference data from the literature that were obtained with comparable methods and are summarized in Table I. Intensity ratios observed at temperatures up
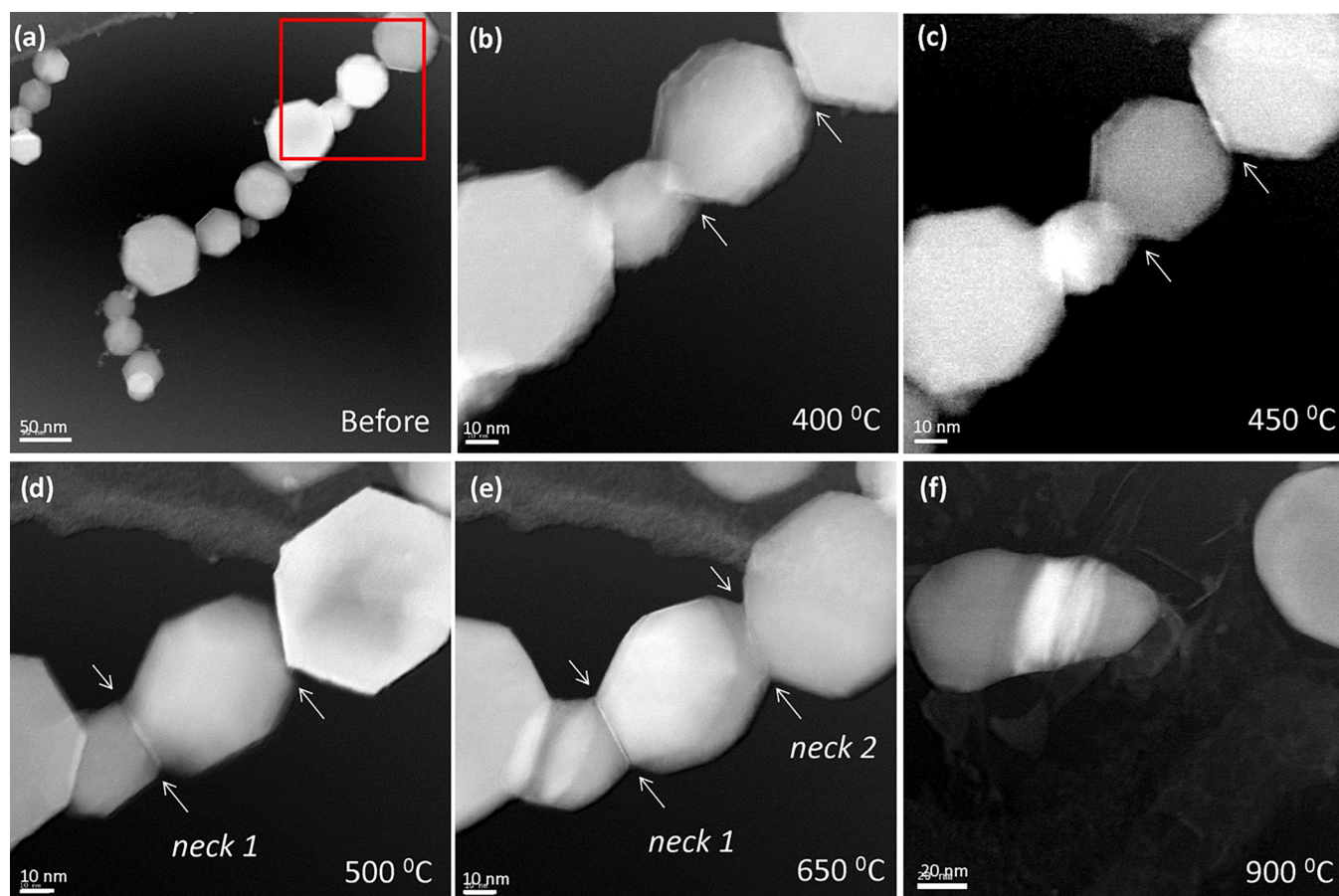
FIG. 4. Series of HAADF images of the particles marked in (a) acquired during *in situ* heating above 400 °C. A rough surface morphology can be observed up to 450 °C (b) and (c), before transitioning to rather smooth surfaces at 500 °C (d). Beginning at 500 °C, necks form between adjacent particles (d) and (e). At 900 °C (f), consolidated nanochains were observed.

to 200 °C reveal excellent agreement with reference data for γ-Fe$_2$O$_3$.[27,29,32] In the temperature range between 200 °C and 450 °C, the experimental data match those observed for Fe$_3$O$_4$.[27,29] Intensity ratios between 3.5 and 4.3 for the temperature interval from 450 °C and 800 °C reproduce those observed for FeO,[27,32] while smaller values at higher temperatures indicate a transition from FeO to metallic Fe.[33]

IV. DISCUSSION

In situ heating experiments in the TEM have revealed significant changes in the morphology and electronic structure for nanochains that are comprised of 1-dimensionally aligned iron oxide nanoparticles. Gradual heating within the TEM column that is operated at an oxygen partial pressure of $pO_2 = 7 \times 10^{-9}$ mbar creates a reducing environment. The ELNES results for the Fe L$_{2,3}$ edges presented in Sec. III B demonstrate significant drops in the L$_3$/L$_2$ intensity ratios, which indicate reduction-oxidation reactions as a function of temperature that coincides with neck formation between and coalescence of adjacent particles.

A. Reduction-oxidation reactions

The gradual shift of the edge onset for the Fe L$_{2,3}$ edges (cf. Fig. 5) indicates a core level shift often observed during reduction-oxidation reactions, i.e., phase transformations in

3d transition metal oxides.[33] This observation suggests that the γ-Fe$_2$O$_3$ nanoparticles stable at room temperature were reduced to FeO below 600 °C. The analysis of L$_3$/L$_2$ intensity ratios extracted from Fe L$_{2,3}$ ELNES is a suitable tool to evaluate the oxidation state of iron as a function of annealing temperature during the *in situ* heating experiments. Comparing the Fe L$_3$/L$_2$ intensity ratios plotted in Fig. 5(b) with values reported in the literature (see Table I) indeed indicates the reduction of the γ-Fe$_2$O$_3$ phase to Fe$_3$O$_4$, FeO, and subsequently metallic Fe.

Above 200 °C, L$_3$/L$_2$ intensity ratios obtained from the center of the particles were indistinguishable from those at the particle surfaces. At room temperature, the surface of the particles appears more consistent with FeO composition, which reproduces earlier results by Jasinski *et al*. Heating to 200 °C leads to surface oxidation toward Fe$_2$O$_3$ likely due to the flux of oxygen ions from the center toward the surface of the particles, which describes the kinetic mechanism of the overall reduction of the iron oxide particles. L$_3$/L$_2$ intensity ratios drop from values above 5.5 to around 5.2 at 200 °C, which represents a phase transition from γ-Fe$_2$O$_3$ with a +III oxidation state for iron to the inverse spinel structure of Fe$_3$O$_4$. The observed intensity ratios between 200 °C and 450 °C correlate well with the corresponding reference data in Table I. Decreasing ratios up to 350 °C and constant values between 350 °C and 450 °C [cf. Fig. 5(b)] suggest a gradual transition
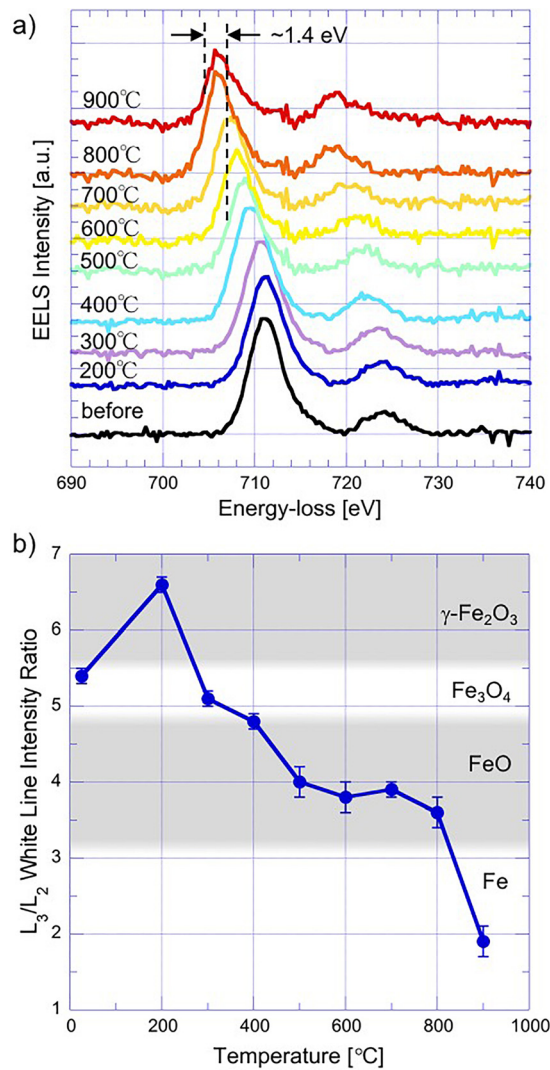
a)

b)

FIG. 5. (a) EELS Fe $L_{2,3}$ ionization edges recorded from the iron oxide nanochains during *in situ* heating experiments. The onset of the L_3 edge shifts by 1.4 eV toward lower energy losses in the temperature range between 500 °C and 900 °C. (b) is a plot of the extracted Fe L_3/L_2 white line intensity ratios as a function of temperature. Bulk iron oxide phases were assigned according to reference values from the literature listed in Table I.

from the characteristic mixed Fe^{II+} and Fe^{III+} valence states to Fe^{II+}, hence representing a phase transition from Fe_3O_4 to FeO. Above 500 °C, some discrepancies in the intensity ratios with the reference data were identified. The observed intensity ratios for 500 °C, 600 °C, and 800 °C of 4.0, 3.5, and 3.4,

TABLE I. EELS Fe L_3/L_2 ratio values of iron oxide from different references in the literature.

Fe L_3/L_2 ratio$_{ref}$	Assigned phase
6.5 ± 0.3	α-Fe_2O_3 (Ref. 32)
6.0 ± 0.3	α-Fe_2O_3 (Ref. 30)
5.8 ± 0.3	γ-Fe_2O_3 (Ref. 32)
5.5 ± 0.3	γ-Fe_2O_3 (Refs. 28 and 30)
5.2 ± 0.3	Fe_3O_4 (Refs. 30 and 32)
4.6 ± 0.3	FeO (Ref. 32)
4.4 ± 0.3	FeO (Ref. 28)
4.1	FeO (Ref. 33)
3.0	Fe (Ref. 33)

respectively, are smaller than those expected for FeO, i.e., 4.6 ± 0.3 (Ref. 32) and 4.4 ± 0.3.[27] While such ratios may be identified with metallic Fe, EELS spectra between 500 °C and 800 °C exhibited the presence of the O K absorption edge (see supplementary material S1). According to Leapman and co-workers, the recorded chemical shift of 1.4 eV towards lower energy losses between 500 °C and 900 °C is in excellent agreement with a transformation of FeO to metallic Fe.[33] Therefore, FeO was considered as the oxide phases in this temperature interval. Lattice fringes observed in annular dark-field STEM images further corroborate this finding. Figure 6 shows micrographs of different areas of a nanochain acquired during in-situ heating experiments at 650 °C and 700 °C, respectively. The areas indicated in both images were Fourier filtered, and the extracted lattice spacing of 0.237 ± 0.030 nm and 0.213 ± 0.040 nm is in excellent agreement with those for the (111) and (200) planes in FeO, respectively. The L_3/L_2 observed at 900 °C is significantly smaller than those observed at lower temperatures [see Fig. 5(b)]. In this case, metallic iron was selected as the assigned phase because no oxygen signal was detected in the acquired EELS spectra (see Fig. S2 in the supplementary materials).

The quantification of L_3/L_2 intensity ratios is subject to specific processing parameters during data analysis, such as widths of integration windows and continuum background fitting.[27] As a consequence, absolute L_3/L_2 intensity ratios often reveal variations for the exact same sample. However, relative changes within the same study are self-consistent and provide reliable information about a variation in 3d transition metal oxidation states.[33,34]

The observation of the wüstite phase, i.e., FeO, was unexpected on the nanoscale since Navrotsky and co-workers have predicted a thermodynamically driven shift in the phase equilibria.[21] Under ultra-high vacuum conditions ($pO_2 \approx 10^{-23}$ mbar), bulk FeO is stable with respect to Fe_3O_4 above 560 °C,[35,36] while Fe_3O_4 nanoparticles smaller than 10 nm are in direct equilibrium with metallic Fe at 727 °C.[21] Considering the oxygen partial pressure in the TEM utilized for this study ($pO_2 \approx 7 \times 10^{-9}$ mbar), the bulk transition temperatures for Fe_2O_3 to Fe_3O_4 and Fe_3O_4 to FeO change to approximately 627 °C and 1027 °C, respectively. However, the experimentally observed transition temperatures around 200 °C and 450 °C, respectively, are significantly smaller, which is attributed to the nanoscale dimensions of the nanochains. The transition temperatures observed in this study are consistent with those from previous *in situ* X-ray diffraction experiments of iron oxide thin films.[37,38] Although the effects of electron beam damage during *in situ* TEM studies, such as oxygen vacancy formation, cannot be neglected for this study, the observed systematic reduction of iron oxide nanochains is in good agreement with previous studies. *In-situ* TEM heating experiments of individual iron oxide nanoparticles under the same conditions reported in this study have revealed the elimination of the FeO phase, and demonstrate equilibrium between Fe_3O_4 and metallic Fe.[39]

B. Surface morphology

During *in situ* heating experiments, the iron oxide nanoparticles within the nanochains exhibited a smooth-to-rough
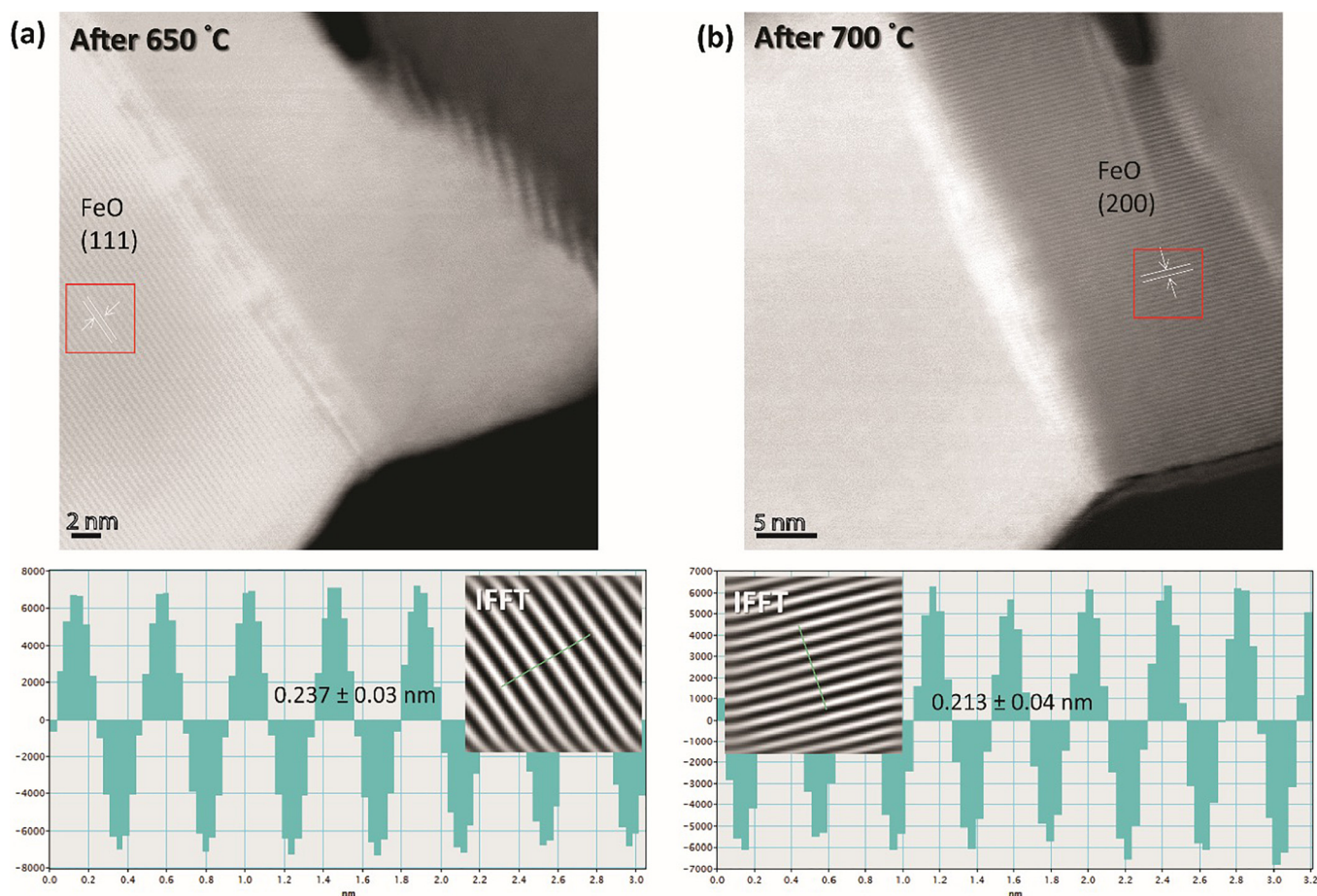
FIG. 6. Annular dark field STEM images recorded after annealing at (a) 650 °C and (b) 700 °C. Both images reveal lattice fringes. Fourier analysis of the marked areas reveals lattice fringes with a spacing of 0.237 ± 0.030 and 0.213 ± 0.040 nm that are consistent with the interplanar lattice distances for (111) and (200) planes in FeO, respectively.

transition of the surface morphology at relatively low temperatures below 300 °C, and subsequent rough-to-smooth transitions around 500 °C (see Figs. 3 and 4). Temperature dependent surface roughening is often observed for metal[40] and ceramic nanoparticles.[41] In this study, changes in the observed surface morphology are attributed to the identified phase changes, i.e., oxygen stoichiometry. Surface roughening below 300 °C is concluded to be caused by the surface reduction of γ-Fe$_2$O$_3$, as indicated by the crater-like surface structures in Fig. 3. Similar effects were previously observed during the *in situ* heating of NiO[13] and aluminum nanoparticles.[41]

The reverse rough-to-smooth transformation above 500 °C is likely caused by the transition from the Fe$_3$O$_4$ phase characterized by coexisting +II and +III oxidation states for Fe, to FeO with only Fe^{+II}. For FeO, reported surface energies are considerably larger than those for Fe$_3$O$_4$,[21] which relates to significantly higher roughening temperatures for FeO and, thus, the formation of smooth surface morphologies above 500 °C.

C. Coalescence and densification

A series of reduction-oxidation reactions induced by *in situ* heating have triggered coalescence and densification of the iron oxide nanochains. Unlike volume sintering on much larger length-scales, coalescence and densification commenced

by surface diffusion once Fe^{II+} valency was established.[22] The oxygen-to-iron ionic ratio approaches unity during cation reduction, which promotes the formation of cation vacancies and, thus, surface diffusion.[22,42] After initial partial reduction of γ-Fe$_2$O$_3$ to Fe$_3$O$_4$, the inverse spinel structure of magnetite transformed to FeO crystallizing in the rock salt structure, resulting in increased cation diffusion to fill vacant lattice sites while the oxygen lattice remains mostly unchanged.[25] The re-emerging smooth surface morphology was observed concurrently with the first neck formation [see Fig. 4(d)], and a change in the surface curvature [cf. Figs. 3 and 4(c) and 4(d)]. The variation in the mean curvature of the particles causes a chemical potential gradient, which is the driving force for the initial stage of sintering.[43]

The proposed requirement for Fe^{+II} to initiate coalescence and eventually densification is consistent with previous sintering studies for Fe$_2$O$_3$ and Fe$_3$O$_4$. Isothermal heating of Fe$_2$O$_3$ powders at 300 °C in vacuum did not lead to densification,[44] while fine grained and uniform microstructures were obtained after pre-treating the same powders and sintering at 1200 °C.[45] SPS was employed to densify Fe$_2$O$_3$ nanoparticles to similar densities under uniaxial pressure and at temperatures as low as 300 °C–350 °C.[46] In comparison, Fe$_3$O$_4$ powders were sintered at 500 °C in vacuum and 570 °C in air.[22] The latter study illustrates that the increased presence of Fe^{II+} in vacuum enhances consolidation due to the reducing environment.

V. CONCLUSION

In this study, *in situ* TEM experiments were utilized to gradually heat 1-dimensional nanochains of γ-Fe$_2$O$_3$ nanoparticles to explore the correlation between oxidation-reduction reactions and particle coalescence. With increasing temperatures, a gradual reduction to Fe$_3$O$_4$, FeO, and subsequently metallic iron was observed by electron energy loss spectroscopy. Simultaneous imaging of nanochains at different temperatures revealed surface roughening for the phase transition from γ-Fe$_2$O$_3$ to Fe$_3$O$_4$, while smooth surfaces were obtained after phase transformation to FeO, which also coincided with inter-particle neck formation and, ultimately, coalescence. The correlation of roughening transitions with apparent phase transitions identified by changes in cation valency indicates that Fe^{+II} cations are required for sufficient surface diffusion that initiates neck formation. The unexpected existence of a stable iron(II)oxide phase, i.e., FeO or Wüstite, indicates the potential for its phase stabilization on the nanoscale due to the nanochain morphology.

SUPPLEMENTARY MATERIAL

See supplementary material for energy-loss spectroscopy data of the O K-edge as a function of temperature to verify the presence and subsequent absence of oxygen in FeO and metallic iron, respectively.

ACKNOWLEDGMENTS

[1] S.-J. L. Kang, *Sintering: Densification, Grain Growth, and Microstructure* (Elsevier Butterworth-Heinemann, 2005).
[2] R. Chaim, J. Mater. Sci. **48**, 502 (2013).
[3] V. Y. Kodash, J. R. Groza, K. C. Cho, B. R. Klotz, and R. J. Dowding, Mater. Sci. Eng. A **385**, 367 (2004).
[4] J. R. Groza, M. Garcia, and J. A. Schneider, J. Mater. Res. **16**, 286 (2001).
[5] J. R. Groza and A. Zavaliangos, Mater. Sci. Eng. A **287**, 171 (2000).
[6] G. Q. Xie, O. Ohashi, N. Yamaguchi, M. Song, K. Mitsuishi, K. Furuya, and T. Noda, J. Mater. Res. **19**, 815 (2004).
[7] N. Sato, Electrochim. Acta **16**, 1683 (1971).
[8] Z. A. Munir, J. Mater. Sci. **14**, 2733 (1979).
[9] G. Aldica, V. Khodash, P. Badica, and J. R. Groza, J. Optoelectron. Adv. Mater. **9**, 3863 (2007).
[10] T. B. Holland, U. Anselmi-Tamburini, T. B. Tran, D. V. Quach, J. R. Groza, and A. K. Mukherjee, J. Eur. Ceram. Soc. **32**, 3659 (2012).
[11] C. S. Bonifacio, T. B. Holland, and K. van Benthem, Scr. Mater. **69**, 769 (2013).
[12] C. S. Bonifacio, J. F. Rufner, T. B. Holland, and K. van Benthem, Appl. Phys. Lett. **101**, 093107 (2012).
[13] M. Matsuno, C. S. Bonifacio, J. F. Rufner, A. M. Thron, T. B. Holland, A. K. Mukherjee, and K. van Benthem, J. Mater. Res. **27**, 2431 (2012).
[14] D. K. Bora, A. Braun, S. Erat, O. Safonova, T. Graule, and E. C. Constable, Curr. Appl. Phys. **12**, 817 (2012).
[15] A. K. Gupta, R. R. Naregalkar, V. D. Vaidya, and M. Gupta, Nanomedicine **2**, 23 (2007).
[16] S. Laurent, D. Forge, M. Port, A. Roch, C. Robic, L. Vander Elst, and R. N. Muller, Chem. Rev. **108**, 2064 (2008).
[17] Q. Liu, Z.-M. Cui, Z. Ma, S.-W. Bian, W.-G. Song, and L.-J. Wan, Nanotechnology **18**, 385605 (2007).
[18] Z. Jing, Y. Wang, and S. Wu, Sens. Actuators, B **113**, 177 (2006).
[19] A. K. Gupta and M. Gupta, Biomaterials **26**, 3995 (2005).
[20] D. K. Bora and P. Deb, Nanoscale Res. Lett. **4**, 138 (2009).
[21] A. Navrotsky, C. Ma, K. Lilova, and N. Birkner, Science **330**, 199 (2010).
[22] C. M. Kramer and R. M. German, J. Am. Ceram. Soc. **61**, 340 (1978).
[23] J. R. Wynnyckyj and T. Z. Fahidy, Metall. Trans. **5**, 991 (1974).
[24] D. W. Sterner and H. D. Merchant, J. Mater. Sci. **8**, 1823 (1973).
[25] S. Prakash, J. South. Afr. Inst. Min. Metall. **96**, 3 (1995).
[26] L. F. Allard, W. C. Bigelow, M. Jose-Yacaman, D. P. Nackashi, J. Damiano, and S. E. Mick, Microsc. Res. Tech. **72**, 208 (2009).
[27] J. Jasinski, K. E. Pinkerton, I. M. Kennedy, and V. J. Leppert, Microsc. Microanal. **12**, 424 (2006).
[28] R. F. Egerton, *Electron Energy Loss Spectroscopy in the Electron Microscope*, 2nd ed. (Plenum Press, New York, 1996).
[29] D. H. Pearson, B. Fultz, and C. C. Ahn, Appl. Phys. Lett. **53**, 1405 (1988).
[30] Y.-M. Zhou, C.-Y. Zhong, I. M. Kennedy, V. J. Leppert, and K. E. Pinkerton, Toxicol. Appl. Pharmacol. **190**, 157 (2003).
[31] G. K. Das, C. S. Bonifacio, J. De Rojas, K. Liu, K. van Benthem, and I. M. Kennedy, J. Mater. Chem. A **2**, 12974 (2014).
[32] C. Colliex, T. Manoubi, and C. Ortiz, Phys. Rev. B **44**, 11402 (1991).
[33] R. D. Leapman, L. A. Grunes, and P. L. Fejes, Phys. Rev. B **26**, 614 (1982).
[34] C. Scheu, W. Stein, and M. Rühle, Phys. Status Solidi **222**, 199 (2000).
[35] R. A. Robie and B. S. Hemingway, Thermodynamic properties of minerals and related substances at 298.15 K and 1 Bar (10^5 Pascals) pressure and at higher temperatures, U.S. Geol. Survey Bull. **2131**, 461 (1995).
[36] L. S. Darken and R. W. Gurry, J. Am. Chem. Soc. **67**, 1398 (1945).
[37] G. Ketteler, W. Weiss, W. Ranke, and R. Schlögl, Phys. Chem. Chem. Phys. **3**, 1114 (2001).
[38] F. Bertram, C. Deiter, K. Pflaum, M. Suendorf, C. Otte, and J. Wollschläger, J. Appl. Phys. **110**, 102208 (2011).
[39] C. B. Fittz, H. Majidi, and K. van Benthem, Microsc. Microanal. **23**, 1718 (2017).
[40] T. B. Holland, A. M. Thron, C. S. Bonifacio, A. K. Mukherjee, and K. van Benthem, Appl. Phys. Lett. **96**, 243106 (2010).
[41] G. D. Förster, M. Girault, J. Menneveux, L. Lavisse, J.-M. Jouvard, V. del Carmen Marco de Lucas, V. Potin, F.-X. Ouf, M. Kerkar, J.-L. Le Garrec, E. Carvou, S. Carles, F. Rabilloud, F. Calvo, J. Yu, and J. B. Mitchell, Phys. Rev. Lett. **115**, 246101 (2015).
[42] B. Gillot, J. F. Ferriot, and A. Rousset, J. Phys. Chem. Solids **37**, 857 (1976).
[43] R. M. German and Z. A. Munir, J. Am. Ceram. Soc. **59**, 379 (1976).
[44] R. I. Razouk, R. S. Mikhail, and B. S. Girgis, in *Solid Surfaces*, edited by L. E. Copeland, R. A. Beebe, D. P. Graham, A. C. Zettlemoyer, and W. A. Zisman (American Chemical Society, Washington, DC, 2009), pp. 42–50.
[45] H.-I. Hsiang and F.-S. Yen, Ceram. Int. **29**, 1 (2003).
[46] P. Saravanan, J.-H. Hsu, D. Sivaprahasam, and S. V. Kamat, J. Magn. Magn. Mater. **346**, 175 (2013).